PAPER

Photoinduced enhancement of a triboelectric nanogenerator based on an organolead halide perovskite

Li Su,†[a] Zhenxuan Zhao,†[b] Huayang Li,[a] Ying Wang,[a] Shuangyang Kuang,[a] Guozhong Cao,[c] Zhonglin Wang[ad] and Guang Zhu*[a]

We report a methylammonium lead triiodide (MAPbI$_3$) perovskite-based photoenhanced triboelectric nanogenerator (TENG). It features a dual working mechanism that relies on the joint properties of the photoelectric and triboelectric effects of the perovskite material. Both the photoconductivity and the surface triboelectric density of the perovskite-based composite thin film are significantly altered under solar illumination, resulting in considerable enhancement of the electrical output. The triboelectric output open-circuit voltage (V_{oc}), short circuit current (I_{sc}), and amount of electric charge (Q) were increased by 11%, 11%, and 9%, respectively, after illumination under full-sun conditions. Our work provides an approach for the enhancement of the mechanical-to-electrical conversion efficiency of the TENG by sunlight absorption.

1. Introduction

Harvesting energy in forms such as mechanical,[1] thermal,[2] magnetic,[3] light,[4] and chemical[5] energy from ambient sources is attracting world-wide attention because of the rapid development of small portable electronics, self-powered systems, and wireless sensing networks. Among the techniques for mechanical energy harvesting, triboelectric nanogenerators (TENGs) have been shown to be advantageous because of their high output power density, high conversion efficiency, low cost, and diverse materials options.[6–10] A major current research interest in this area focuses on improving the device output power through approaches such as material modification,[11] structural design and optimization,[12] and the use of a hybrid energy-harvesting mechanism.[13] In particular, the hybrid route involves converting other energy sources other than mechanical motions by incorporating corresponding energy-conversion means into a TENG.[14–16] For example, the photoelectric/triboelectric hybrid TENG simultaneously targets mechanical energy and optical energy. In previous reports, the mechanical energy and optical energy were harvested by individual components that performed separately with at most three electrodes in common. The individual components produced corresponding electrical outputs that were superimposed through the use of additional circuit rectifiers, as shown in Table 1.[17–20] Hence, the development of a single-structured and multifunctional hybrid TENG without additional electronic components is critical for promoting the practical applications of photoelectric/triboelectric hybrid nanogenerators.

Recently, methylammonium lead triiodide organometal halide (MAPbI$_3$) perovskite has attracted tremendous attention because of its excellent light absorption capability.[21–23] In this report, we present a new approach to demonstrate photoinduced enhancement of a TENG based on perovskite. The perovskite serves as not only a triboelectrification material but also a photon-absorbing material. In the absence of illumination, the perovskite-based TENG with lateral dimensions of 2.0 × 2.0 cm^2

[a] Beijing Institute of Nanoenergy and Nanosystems, Chinese Academy of Sciences, National Center for Nanoscience and Technology (NCNST), Beijing, 100083, China. E-mail: zhuguang@binn.cas.cn

[b] Institute of Microelectronics, Tsinghua University, Beijing, 100084, China

[c] Department of Materials and Engineering, University of Washington, Seattle, WA98195-2120, USA

[d] School of Materials Science and Engineering, Georgia Institute of Technology, Atlanta, GA 30332, USA. E-mail: zlwang@binn.cas.cn

† These authors contributed equally to this work.

Table 1 Previous reports on the photoelectric/triboelectric hybrid nanogenerators

	Materials (SC)	Materials (TENG)	Electrical rectification	No. of components	No. of electrodes
Y. Ya et al.[17]	Si	ITO/PDMS	Yes	1	3
H. Y. Guo et al.[18]	ZnO	Cu/PTFE	Yes	2	3
H. J. Fang et al.[19]	MAPbI$_3$	Cu/PC	Yes	1	3
Y. K. Pang et al.	MoS$_2$	Al/FEP	No	1	3
This work	MAPbI$_3$	Cu/MAPbI$_3$	No	1	2

This journal is © The Royal Society of Chemistry 2016

J. Mater. Chem. C, 2016, 4, 10395–10399 | **10395**

produces voltage and current amplitudes of 15.3 V and 0.29 μA, respectively. Upon illumination with a full-spectrum standard simulated sunlight, the voltage and the current amplitude were increased to 17 V and 0.38 μA, respectively. In this case, triboelectric charge can be supplemented and enhanced by the photogenerated electrons or holes upon illumination. The enhancement mechanism is investigated in detail by using scanning Kelvin probe microscopy (SKPM) and conductive atomic force microscopy (CAFM) measurements. In this approach, no rectification is needed for the photo-enhanced TENG, making it more reliable in terms of low cost and easy operation in the fabrication process. Our results not only demonstrate a new approach to enhancing the TENG output but also represent a new principle in the TENG field.

2. Results and discussion

The structure of the photoenhanced TENG is illustrated in Fig. 1a. $MAPbI_3$ has a distorted tetragonal perovskite structure at room temperature, as shown in Fig. 1b. The photoenhanced TENG based on the perovskite consisted of an upper part and a bottom part (Fig. 1a) with lateral dimensions of 2.0×2.0 cm^2. The bottom part was constructed on a transparent FTO (SnO$_2$:F)-coated glass substrate, and $MAPbI_3$ was deposited onto mesoporous TiO$_2$ scaffolds as an electron transfer layer. The upper part was a polytetrafluoroethylene (PTFE) film pasted onto a sponge layer. A copper layer was deposited onto the back of the PTFE film. The FTO and the copper layer served as the top and the bottom electrodes, respectively. They were connected to the positive and the negative terminals of an electrometer for data acquisition, respectively. The detailed fabrication process is described in the Experimental section. Scanning electron microscopy (SEM) and atomic force microscopy (AFM) were used to characterize the morphology and surface roughness of the perovskite layer. As shown by the SEM image in Fig. 1c, a mesostructured TiO$_2$ layer (300 nm thick),

along with a compact electron-blocking layer (25 nm thick), was filled into crystalline $MAPbI_3$ and capped by $MAPbI_3$ nanoparticles on the top. A SEM top-view of the capping layer is shown in Fig. 1d, which reveals that the layer is composed of $MAPbI_3$ particles with a diameter of *ca*. 200 nm. The surface morphology in Fig. 1e using AFM also reveals an average roughness of 21 nm. The X-ray diffraction (XRD) pattern shown in Fig. 1f agrees well with the tetragonal perovskite structure as previously reported.[24]

The photovoltaic performance of the perovskite was characterized by measuring the short-circuit current density (J_{sc}) and open-circuit voltage (V_{oc}). Fig. 2a shows the current density *vs.* voltage ($J-V$) curves for a perovskite-based solar cell under a full-sun condition. The J_{sc}, V_{oc}, device area, FF, and PCE values of 19.8 mA cm^{-2}, 0.97 V, 3.5 cm^{-2}, 63, and 12.29% were obtained, respectively. The photoenhanced TENG is essentially a TENG that can convert mechanical energy into electricity. When an external force brings the PTFE layer into repeated contacts with the perovskite layer, triboelectric charges of opposite signs on the contact surfaces induce an oscillating V_{oc} between the two electrodes, as shown in Fig. 2b. The measurable voltage is ascribed to the electric potential difference between the two electrodes.

The electric output of the TENG was measured as it was repeatedly illuminated with full-spectrum switchable standard simulated sunlight for four cycles. The obtained V_{oc} is shown in Fig. 3a. The reciprocating mechanical motion applied by the linear motor produced an ac-type voltage signal. The average voltage amplitude (peak-to-peak value) was 15.3 V, corresponding to the electric output produced by the TENG. Once the light source was turned on, the voltage amplitude increased considerably and reached an average value of 17 V, representing an enhancement of 11%. Upon removal of the light source, the voltage amplitude immediately recovered to its original value. The four cycles of the periodic illumination indicate excellent repeatability of the photo-enhancement. A magnified view of the voltage in Fig. 3a reveals a rapid response characterized by a response time of less than 250 ms. In addition to the voltage, similar photoenhanced enhancement was observed in the short-circuit current (I_{sc}) and in the charge quantity (Q), as shown in Fig. 3b and c, respectively. I_{sc} with an amplitude of 0.29 μA in darkness increased to 0.38 μA upon illumination. Correspondingly, Q was enhanced from 5.7 nC to 6.2 nC as a result of illumination. The enhancement of Q was calculated by
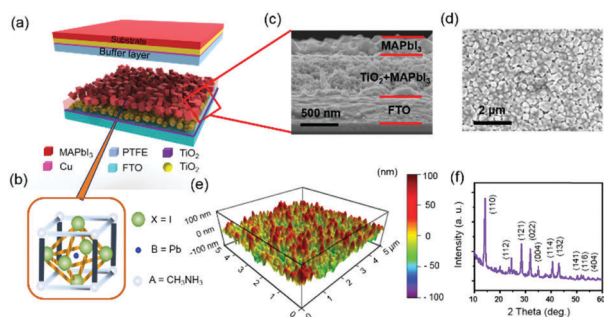

Fig. 1 (a) Device structure of the photoenhanced TENG. Note: the device working processes are contact and separation modes with a 2.0 × 2.0 cm^2 active area. (b) Three-dimensional schematic representation of the MAPbI$_3$ perovskite structure. (c) Cross-sectional SEM images of the perovskite-based film, including the MAPbI$_3$ capping layer (~250 nm thickness), mesoporous TiO$_2$ filled with MAPbI$_3$, the compact TiO$_2$ layer, and the FTO substrate. (d) Surface-sectional SEM images of the perovskite-based film. (e) Three-dimensional AFM image of the MAPbI$_3$ capping layer. The average surface roughness is 21 nm. (f) XRD pattern of the perovskite-based film.
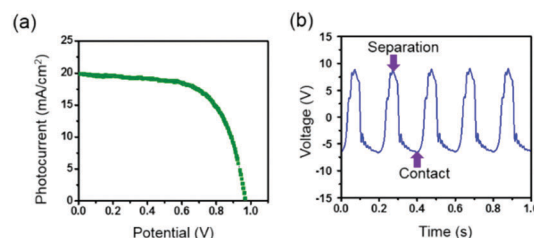

Fig. 2 Typical electrical output signals of the solar cell and the TENG fabricated using the perovskite material. (a) $J-V$ curve of the perovskite solar cell under the full-sun condition. (b) Open-circuit voltage (V_{oc}) of the photoenhanced TENG without illumination.
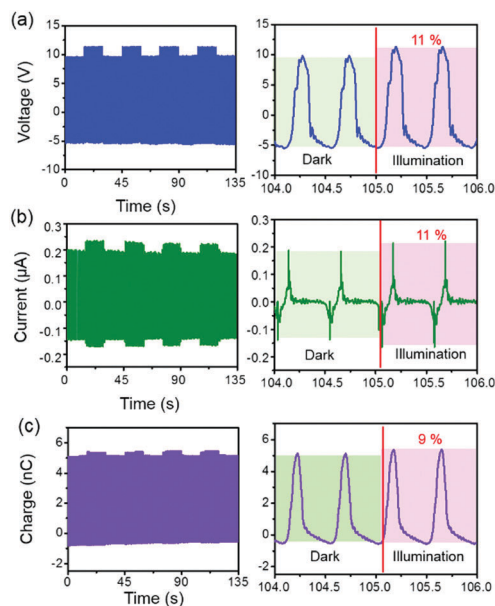
10396 | *J. Mater. Chem. C*, 2016, **4**, 10395–10399

This journal is © The Royal Society of Chemistry 2016

Fig. 3 Measured time dependence of the (a) V_{oc}, (b) short-circuit current (I_{sc}), and (c) amount of electric charge (Q) of the photoenhanced TENG under switchable standard simulated sunlight illumination, and the corresponding magnified views at the moment of the illumination.

the difference of the amplitude value. But for the current, the enhancement should be expressed as the integral area of the current vs. time (I–V) curve. Thus, the enhancement of Q and I_{sc} was 9% and 11%, respectively. The corresponding enlarged views in Fig. 3b and c also show rapid response characteristics.

To investigate the mechanism of the enhancement in the obtained electric signals, we used SKPM to characterize the surface charge transfer at nanoscale.[25] Unlike the contact-mode of atomic force microscopy (AFM), SKPM detects the potential

difference between a sample surface and a probe tip driven by an applied AC bias in the lift mode. We characterized the surface potential of a targeted area with dimensions of $5 \times 5~\mu m^2$ by SKPM using a Pt-coated Ir probe. The trapping amplitude was set to 3 V at a lift height of 100 nm. Prior to the measurement, the perovskite surface was manually rubbed with the PTFE surface for multiple cycles. Fig. 4a shows the 3D surface potential distribution on the perovskite surface area at different states in a sequential order. Compared to the state before rubbing, the surface potential after 5 min of rubbing increased from 220 to 580 mV. This increase results from the generation of positive surface charge on the perovskite surface due to triboelectrification, as shown in Fig. 4b. Subsequently, the perovskite sample was illuminated at a power density of 70 mW cm^{-2}, as shown in Fig. 4c. Immediately upon illumination, the surface potential rapidly jumped to 730 mV. As the illuminated sample was illuminated for another 10 min, the surface potential decayed to 222 mV, as illustrated in Fig. 4d. This decay is attributed to dissipation of the surface triboelectric charge over time. Because the perovskite material is a semiconductor, it is rather reasonable to suggest that the surface charge was diffused into the material or neutralized by charged particles in ambient air.[26] This decay process was observed to be more rapid than the long-term retention of the triboelectric charge on insulating polymers.[27] The four states are shown quantitatively in Fig. 4e. On the basis of the SKPM results, we constructed a model in which the surface charge density of the perovskite varies upon illumination, as shown in Fig. 4f. Illumination is known to produce a large number of electron–hole pairs on the perovskite surface. Because of the presence of the mesoporous electron-conducting TiO$_2$ scaffold, the generated electrons are then transported away from the perovskite surface, leaving an excess of holes on the illuminated surface. These positively charged
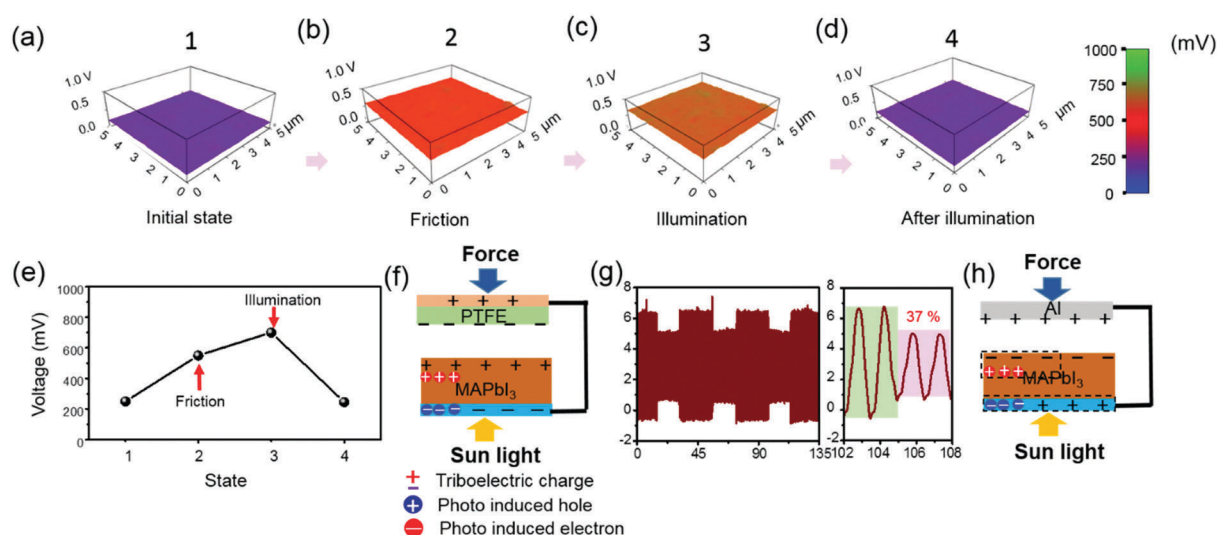

Fig. 4 Surface potential mapping on the perovskite material in its (a) initial, (b) upon friction, (c) upon illumination, and (d) after illumination states. (e) Corresponding values of the surface potentials of the four states. Illustration of separation and migration of triboelectric surface charges and photogenerated e–h pairs of the photoenhanced TENG: (f) PTFE/perovskite–based TENG and (h) Al/perovskite-based TENG. (g) Measurement of the time dependence of V_{oc} of the Al/perovskite-based TENG.
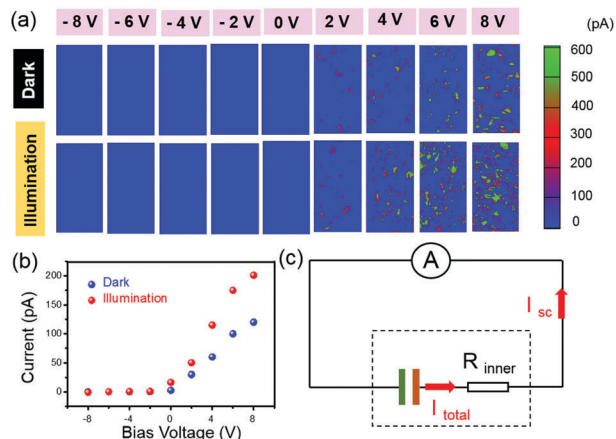
Fig. 5 (a) Current distribution mapping of the perovskite-based layer with bias voltages from −8 to +8 V at an increment of 2 V in darkness and upon illumination (power density of 70 mW cm^{-2}). (b) I–V characteristics of the perovskite-based layer. (c) Equivalent electrical diagram for measuring the I_{sc} of the photoenhanced TENG.

holes, in turn, add to the already-existing positive triboelectric charge, resulting in an increase of the measured surface potential. To further justify the proposed mechanism above, we constructed a control device with a different structure. For simplification, the top part of the TENG was fabricated using Al films instead of PTFE. The Al film acts as both the top electrode and the top triboelectric layer. As shown in Fig. 4g, because of the extremely strong electron accepting ability, the tribocharges on the Al films were positive, leaving negative charges on the perovskite side after rubbing. The voltage change under repetitive switchable illumination was opposite to that of the photoenhanced TENG, indicating that the negative triboelectric surface charges at the perovskite surface were neutralized by the photogenerated holes under illumination, resulting in the reduction of the electrical output, as shown in the working mechanism presented in Fig. 4h. These results provide further evidence of the aforementioned model of the enhanced TENG.

For the semiconducting characteristics of the perovskite, we propose that the change of conductivity upon illumination also contributed to the enhancement of the TENG output. Here, we used CAFM measurements to investigate the photoconductive behavior of the perovskite-based layer. In this experiment, we recorded the current induced by bias voltage applied onto the FTO substrate. The illumination was aligned with the tip in an inverted optical lens. The tip–sample contact force was maintained at 10 nN, which is the minimum value for topography tracking. Fig. 5a shows current distribution maps in darkness and under illumination for the perovskite layer at various bias voltages (−8 to +8 V in 2 V increments). Under a negative bias voltage, very low conductivity values were observed regardless of whether the sample was illuminated. This result indicates that the electrons could only be transported away from the upper part to the bottom of the perovskite, which is consistent with the electron transport characteristic of mesoporous TiO$_2$. In contrast, at a positive bias voltage, the increase in the photocurrent suggested the same transport behavior. However, it was observed that the

current upon illumination was much higher than that in darkness even if the same positive bias voltage was applied. The current exhibited an increase as large as two-fold under a +8 V bias voltage, indicating a substantial enhancement in conductivity. The relative I–V characteristics of the perovskite-based layer are shown in Fig. 5b. The significant enhancement in conductivity upon illumination demonstrated by the CAFM measurements would lead to a decrease in the inner resistance of the TENG, and thus to an enhancement of the photo-enhanced TENG output, as shown in Fig. 5c.

3. Conclusion

In conclusion, we have demonstrated that the perovskite-based TENG enhancement can be realized under sunlight illumination. The total output was enhanced because of the varying surface charge density and conductivity of the perovskite upon illumination. The working mechanism of the TENG was discussed in detail in terms of SKPM and CAFM measurements. These results will aid further investigations in the TENG field and facilitate the widespread application of photosensitive perovskite materials.

4. Experimental

The perovskite-based film with the configuration of FTO /compact TiO$_2$/mesoporous TiO$_2$ + MAPbI$_3$/MAPbI$_3$ crystalline capping layer was prepared according to the following procedures. Typically, FTO glass substrates were cleaned with detergent and subsequently sonicated in acetone and ethanol. An O$_2$ plasma cleaner was then used to remove organic contaminants for 20 min under 200 Hz. A compact TiO$_2$ blocking layer was deposited onto the cleaned FTO substrate by atomic layer deposition (Picosun SUNALE R-100). TiCl$_4$ and N$_2$ were used as the Ti source and the purge gas, respectively. A compact TiO$_2$ layer with a thickness of 25 nm was grown on the FTO substrate by 500 cycles at a deposition temperature of 200 °C. TiO$_2$ paste (Dyesol-18NRT) was diluted with ethanol in a 2 : 7 weight ratio, spin-coated onto the compact TiO$_2$ layer at 5500 rpm, and sintered at 500 °C for 30 min to form a mesoporous TiO$_2$ layer with 300 nm thickness. PbI$_2$ in DMF solution (462 mg ml^{-1}) was infiltrated into the mesoporous TiO$_2$ layer by spin-coating at 6500 rpm. The TiO$_2$ layer was subsequently dried at 70 °C. After drying, it was dipped into a MAPbI solution (9 mg ml^{-1} in 2-propanol) for 30 s and then sintered at 70 °C for 30 min. We controlled the crystal size of the MAPbI$_3$ capping layer by changing the concentration of the MAI in the solution.

The surface morphology, cross-section, and crystal structure of the as-fabricated perovskite-based composite film were characterized by SEM (Shimadzu, 2020), AFM (MFP-3D SPM), and XRD (X pert 3), respectively. A UV-Vis-NIR spectrophotometer (Shimadzu, UV-3600) was used to analyze the light absorption properties of the perovskite-based film.

The photoenhanced TENG was fabricated in two parts. On one side, acrylic substrates with dimensions of 2.0 × 2.0 × 0.2 cm^3 were prepared by laser cutting. A 200 nm thick copper layer was deposited by magnetron sputtering as the top triboelectric layer

10398 | J. Mater. Chem. C, 2016, 4, 10395–10399

This journal is © The Royal Society of Chemistry 2016

and the top electrode. On the other side, mesoporous TiO_2 and $MAPbI_3$ were prepared on an FTO glass substrate with dimensions of 2.0×2.0 cm^2. Subsequently, two pieces of polyimide films with dimensions of $3.0 \times 2.0 \times 0.125$ cm^3 were prepared and attached to the substrates at the opposite edges. These films served as braces that created a gap between the two contact surfaces. Finally, a conducting wire was connected to each of the electrodes for measurement.

V_{oc} values were measured with a Keithley 6517A electrometer under solar spectrum illumination (AM 1.5, $\sim$100 mW cm^{-2}) with a solar simulator. The CAFM and SKPM experiments were conducted in an Asylum Research MFP-3D atomic force microscope under an ambient environment in CAFM and SKPM modes, respectively. A model EFM-10 (Nanoworld) Ir-based probe with a Pt coating was used in the experiments.

Acknowledgements

Notes and references

1 A. Erturk, J. Hoffmann and D. J. Inman, *Appl. Phys. Lett.*, 2009, **94**, 254102.
2 T. C. Han, J. J. Zhao, T. Yuan, D. Y. Lei, B. W. Li and C. W. Qiu, *Energy Environ. Sci.*, 2013, **6**, 3537.
3 C. L. Zhang, J. S. Yang and W. Q. Chen, *Phys. Lett. A*, 2010, **374**, 2406.
4 X. Hu, X. D. Zhang, L. Liang, J. Bao, S. Li, W. L. Yang and Y. Xie, *Adv. Funct. Mater.*, 2014, **24**, 7373.
5 Z. X. Cai, F. M. Li, W. Xu, Y. Q. Jiang, F. Luo, Y. R. Wang and X. Chen, *Nano Energy*, 2016, **374**, 2406.
6 G. Zhu, C. F. Pan, W. X. Guo, C. Y. Chen, Y. S. Zhou, R. M. Yu and Z. L. Wang, *Nano Lett.*, 2012, **12**, 4960.
7 G. Zhu, J. Chen, Y. Liu, P. Bai, Y. S. Zhou, Q. S. Jing, C. F. Pan and Z. L. Wang, *Nano Lett.*, 2013, **13**, 2282.
8 N. Y. Cui, J. M. Liu, L. Gu, S. Bai, X. B. Chen and Y. Qin, *ACS Appl. Mater. Interfaces*, 2015, **7**, 18225.
9 X. L. Cheng, B. Meng, X. S. Zhang, M. D. Han, Z. M. Su and H. X. Zhang, *Nano Energy*, 2015, **12**, 19.
10 M. L. Seol, J. W. Han, S. B. Jeon, M. Meyyappan and Y. K. Choi, *Sci. Rep.*, 2015, **5**, 16409.
11 H. Y. Li, L. Su, S. Y. Kuang, C. F. Pan, G. Zhu and Z. L. Wang, *Adv. Funct. Mater.*, 2015, **25**, 5691.
12 X. Chen, S. Y. Xu, N. Yao and Y. Shi, *Nano Lett.*, 2010, **10**, 2133.
13 M. D. Han, X. X. Chen, B. C. Yu and H. X. Zhang, *Adv. Electron. Mater.*, 2015, **1**, 1500187.
14 J. H. Lee, K. Y. Lee, M. K. Gupta, T. Y. Kim, D. Y. Lee, J. Oh, C. Ryu, W. J. Yoo, C. Y. Kang, S. J. Yoon, J. B. Yoo and S. W. Kim, *Adv. Mater.*, 2014, **26**, 765.
15 H. Zhang, S. Zhang, G. Yao, Z. Huang, Y. Xie, Y. Su, W. Yang, C. Zheng and Y. Lin, *ACS Appl. Mater. Interfaces*, 2015, **7**, 28142.
16 K. Y. Lee, D. Kim, J. H. Lee, T. Y. Kim, M. K. Gupta and S. W. Kim, *Adv. Funct. Mater.*, 2014, **24**, 37.
17 Y. Yang, H. Zhang, Y. Liu, Z. H. Lin, S. Lee, Z. Lin, C. P. Wong and Z. L. Wang, *ACS Nano*, 2013, **7**, 2808.
18 H. Y. Guo, X. M. He, J. W. Zhong, Q. Zhong, Q. Leng, C. G. Hu, J. Chen, L. Tian, Y. Xia and J. Zhou, *J. Mater. Chem. A*, 2014, **2**, 2079.
19 H. J. Fang, Q. Li, J. Ding, N. Li, H. Tian, L. J. Zhang, T. L. Ren, J. Y. Dai, L. D. Wang and Q. F. Yan, *J. Mater. Chem. C*, 2016, **4**, 630.
20 Y. K. Pang, F. Xue, L. F. Wang, J. Chen, J. J. Luo, T. Jiang, C. Zhang and Z. L. Wang, *Adv. Sci.*, 2016, **1**, 1500419.
21 C. Bi, Y. B. Yuan, Y. J. Fang and J. S. Huang, *Adv. Energy Mater.*, 2015, **5**, 1401616.
22 Z. Yu and L. C. Sun, *Adv. Energy Mater.*, 2015, **5**, 1500213.
23 T. A. Berhe, W. N. Su, C. H. Chen, C. J. Pan, J. H. Cheng, H. M. Chen, M. C. Tsai, L. Y. Chen, A. A. Dubale and B. J. Hwang, *Energy Environ. Sci.*, 2016, **9**, 323.
24 J. H. Heo, S. H. Im, J. H. Noh, T. N. Mandal, C. S. Lim, J. A. Chang, Y. H. Lee, H. j. Kim, A. Sarkar, M. K. Nazeeruddin, M. Grätzel and S. Il Seok, *Nat. Photonics*, 2013, **7**, 486.
25 Y. S. Zhou, Y. Liu, G. Zhu, Z. H. Lin, C. F. Pan, Q. S. Jing, S. Jing and Z. L. Wang, *Nano Lett.*, 2013, **13**, 2771.
26 H. T. Baytekin, A. Z. Patashinski, M. Branicki, B. Baytekin, S. Soh and B. A. Grzybowski, *Science*, 2011, **333**, 309.
27 S. M. Niu, S. H. Wang, L. Lin, Y. Liu, Y. S. Zhou, Y. F. Hu and Z. L. Wang, *Energy Environ. Sci.*, 2013, **6**, 3576.

This journal is © The Royal Society of Chemistry 2016

J. Mater. Chem. C, 2016, **4**, 10395–10399 | **10399**